PHILOSOPHICAL TRANSACTIONS A

rsta.royalsocietypublishing.org

Research

Cite this article: Blondeaux P, Foti E, Vittori G. 2015 A theoretical model of asymmetric wave ripples. *Phil. Trans. R. Soc. A* **373**: 20140112. http://dx.doi.org/10.1098/rsta.2014.0112

One contribution of 12 to a Theme Issue 'Advances in fluid mechanics for offshore engineering: a modelling perspective'.

Subject Areas:
ocean engineering

Keywords:
coastal bedforms, sediment transport, sedimentary structures

Author for correspondence:
P. Blondeaux
e-mail: paolo.blondeaux@unige.it

A theoretical model of asymmetric wave ripples

P. Blondeaux[1], E. Foti[2] and G. Vittori[1]

[1]Department of Civil, Chemical and Environmental Engineering, University of Genova, Via Montallegro 1, 16145 Genova, Italy
[2]Department of Civil Engineering and Architecture, University of Catania, Viale A. Doria 6, 95125 Catania, Italy

The time development of ripples under sea waves is investigated by means of the weakly nonlinear stability analysis of a flat sandy bottom subjected to the viscous oscillatory flow that is present in the boundary layer at the bottom of propagating sea waves. Second-order effects in the wave steepness are considered, to take into account the presence of the steady drift generated by the surface waves. Hence, the work of Vittori & Blondeaux (1990 *J. Fluid Mech.* **218**, 19–39 (doi:10.1017/S002211209000091X)) is extended by considering steeper waves and/or less deep waters. As shown by the linear analysis of Blondeaux *et al.* (2000 *Eur. J. Mech. B* **19**, 285–301 (doi:10.1016/S0997-7546(90)00106-I)), because of the presence of a steady velocity component in the direction of wave propagation, ripples migrate at a constant rate that depends on sediment and wave characteristics. The weakly nonlinear analysis shows that the ripple profile is no longer symmetric with respect to ripple crests and troughs and the symmetry index is computed as a function of the parameters of the problem. In particular, a relationship is determined between the symmetry index and the strength of the steady drift. A fair agreement between model results and laboratory data is obtained, albeit further data and analyses are necessary to determine the behaviour of vortex ripples and to be conclusive.

1. Introduction

In the coastal region, waves and currents often coexist and generate a complex flow that is characterized by the simultaneous presence of an oscillatory velocity component and a steady velocity component. The bottom shear stresses, which are generated by this complex flow field, shape the bottom and often give

THE ROYAL SOCIETY PUBLISHING

rise to small-scale bedforms (ripples) that, in turn, affect the velocity field, because they increase the bottom roughness. Moreover, the ripples have a large influence on transport phenomena and, in particular, on sediment transport, because their presence leads to an increase of the mixing processes and the suspended load. Therefore, a large number of studies have been devoted to investigate ripple formation and to predict their geometrical characteristics (e.g. [1,2]).

The ripples that are observed on the sea bottom are usually grouped into three main categories: wave ripples, wave-current ripples and current ripples [3]. Wave ripples, which are present when the oscillatory flow generated by sea waves close to the bottom is much larger than the steady velocity component, are characterized by (i) lengths that are a fraction of twice the amplitude of the fluid displacement oscillations close to the bottom [2], (ii) crests sharper than troughs, and (iii) a shape that tends to be symmetric with respect to the crests and troughs. Usually, the ratio between the height h_r^* and length l_r^* of these bottom forms is larger than 0.1 (a list of the more frequent symbols used in the analysis appears in table 1). Moreover, flow separation occurs at their crests together with the generation of coherent vortices that pick up the sediments from the bottom and put them into suspension. However, rolling-grain ripples are also observed, which are characterized by a value of h_r^*/l_r^* smaller than 0.1, such that the flow keeps attached to the bottom.

If strong currents are present, current ripples appear, the characteristics of which are similar to those of the small bedforms that cover river beds. Current ripples have a size similar to that of wave ripples, but their profile is asymmetric, with a gentle up-current slope and a quite steep down-current slope that turns out to be close to the angle of repose.

Finally, when the steady velocity component has the same order of magnitude as the oscillatory component, the so-called wave-current ripples are observed, the characteristics of which are somewhat between those of wave ripples and those of current ripples. The distinguishing geometric feature of wave-current ripples is the asymmetry of their profile. Figure 1 shows the experimental results concerning ripple symmetry index plotted versus the ratio between mass-transport velocity u_s^* and the maximum near-bed orbital velocity U_0^*, both evaluated just outside the bottom boundary layer. The symmetry index of ripples is defined as the ratio between the length l_2^* of the gentle (up-current) side to the length l_1^* of the steep (down-current) side of the bottom bedforms. The data of figure 1 are based on the observations of [5,6], Tietze (personal communication to Allen [7]) and [4]. In figure 1, when the steady velocity component is induced by propagating waves, its value is estimated by means of the theory of [8] ($u_s^* = 3\pi a^{*2}\omega^*/[2L^* \sinh^2(2\pi h^*/L^*)]$). Hence, in this case, the abscissa of figure 1 is equal to $3\pi a^*/[2L^* \sinh(2\pi h^*/L^*)]$, where a^* and L^* are the amplitude and length of the sea waves and h^* is the local water depth. On the other hand, when the steady velocity is induced by the superposition of an unrelated current to waves [9,10], u_s^* is the depth averaged steady velocity. The results plotted in figure 1 indicate that ripples tend to become more asymmetric as the mass transport velocity increases. Moreover, comparing the data of wave ripples with those of wave-current/current ripples, it appears that a unidirectional current unrelated to waves affects ripple asymmetry in much the same way as wave-induced mass transport. The mechanism that controls the formation of wave ripples is well understood, because it was shown that the interaction between the oscillatory flow induced close to the bottom by sea waves and a wavy perturbation of the erodible bottom profile gives rise to a steady streaming, which consists of recirculating cells [11,12]. The strength of the steady velocity component and the shape of the recirculating cells depend on the characteristics of both the sea wave and the bedforms. Because the sediment is driven by the fluid, if the steady velocity component close to the bed is directed from the troughs towards the crests of the bottom undulation, the sediments tend to move in this direction. The tendency of the sediments to pile up at the crests is opposed by gravity, which tends to move the sediment from the crests towards the troughs of the bottom forms. Hence, the growth/decay of the bottom waviness is the result of a competition between these two effects. The process that leads to the appearance of wave ripples and their time development was studied and quantified by means of linear and weakly nonlinear analyses [13–20], and the results are summarized in the review papers of [21,22].

Table 1. Notation. The asterisk denotes a dimensional variable, whereas a symbol without the asterisk denotes a dimensionless variable. An overbar denotes the time average over a wave cycle of a time-dependent function.

a^*	amplitude of the surface monochromatic wave
$a = a^*/L^*$	steepness of the surface monochromatic wave
$\hat{a}$	constant defined by (2.13)
a_1, a_2	coefficients of the Landau–Stuart equation
A	function describing the time development of the amplitude of the ripples
A^+	complex conjugate of A
A_e	value of A at equilibrium
$b = 4.28$	constant appearing in (2.11)
$C_1(\tilde{t}), C_2(\tilde{t}), C_3(\tilde{t})$	time-dependent functions describing the oscillations of the ripple profile taking place during the wave cycle around its average position
$\mathcal{C}(\tau)$	time-dependent function describing the growth/decay of the bottom perturbation in the linear analysis
$\mathcal{C}_1^{(1)}(\tilde{t})$	time-dependent function describing the oscillations of the ripple profile taking place during the wave cycle around its average position
d^*	grain size
$F_d = U_0^*\sqrt{(s-1)g^*d^*} = \sqrt{\psi_d}$	sediment Froude number
F_{dc}	critical value of the sediment Froude number
g^*	gravity acceleration
$G = G_r + iG_i$	time-dependent complex function controlling the growth/decay of the bottom perturbation in the linear analysis
$G_0 = G_{0r} + iG_{0i}$	contribution of $O(\delta^0)$ to G ($G = G_0 + \delta G_1$)
$G_1 = G_{1r} + iG_{1i}$	contribution of $O(\delta^1)$ to G ($G = G_0 + \delta G_1$)
h^*	water depth
h_r^*	ripple height
l_r^*	ripple wavelength
l_1^*	distance of the ripple crest from the preceding trough
l_2^*	distance of the ripple crest from the following trough
L^*	wavelength of the surface monochromatic wave
p	sea bed porosity
q^*	sediment transport rate per unit width
$q = q^*/\sqrt{(s-1)g^*d^{*3}}$	dimensionless sediment transport rate per unit width
$\overline{q}^*$	sediment transport rate averaged over half a cycle
$\tilde{q} = q/Q$	rescaled dimensionless sediment transport rate per unit width (see (2.14))
$\tilde{q}_{00}$	leading-order term of the rescaled dimensionless sediment transport rate per unit width
$\tilde{q}_{10}$	term of δ of the rescaled dimensionless sediment transport rate per unit width
$\tilde{q}_{01}, \tilde{q}_{11}$	functions of the temporal coordinate, appearing in (2.24)
$Q = \hat{a}R_d/(2(1-p)\sqrt{\psi_d}Re^b)$	constant appearing in the sediment transport rate predictor

(*Continued*.)

Table 1. (*Continued.*)

$Re = U_0^* \delta^* / \nu^*$	flow Reynolds number
$R_d = U_0^* d^* / \nu^*$	Reynolds number of the sediment
$s = \rho_s^* / \rho^*$	ratio between sediment and fluid densities
t^*	time coordinate
$t = \omega^* t^*$	dimensionless time coordinate
$\tilde{t} = t + 2\pi\delta\tilde{x}$	wave phase
T^*	period of the monochromatic surface wave
$\mathcal{T} = \epsilon Q \tilde{t}$	rescaled morphodynamic temporal coordinate
(u^*, v^*)	horizontal and vertical velocity components
$(u, v) = (u^*, v^*)/U_0^*$	dimensionless horizontal and vertical velocity components
(u_{00}, v_{00})	leading-order term of the dimensionless velocity expansion (see (2.4))
u_{10}, v_{10}	terms order of δ of the dimensionless velocity expansion (see (2.4))
$\hat{u}_{00}, \bar{u}_{10}, \hat{u}_{10}, \hat{v}_{10}$	functions of the vertical coordinate defined by (2.5)–(2.10)
$\hat{u}_{01}, \hat{v}_{01}, \hat{u}_{11}, \hat{v}_{11}$	functions of the vertical coordinate and of time, appearing in (2.22)
u_s^*	steady velocity component
u_s	dimensionless steady velocity component
U_0^*	amplitude of the velocity oscillations induced by the surface wave close to the bottom
V^*	fluid velocity parallel to the bottom at $y^* = \eta^* + d^*/2$
$V = V^*/U_0^*$	dimensionless fluid velocity parallel to the bottom at $y^* = \eta^* + d^*/2$
(x^*, y^*)	Cartesian coordinate system
$(\tilde{x}, \tilde{y}) = (x^*, y^*)/\delta^*$	dimensionless Cartesian coordinate system
$x = \delta^* \tilde{x}/L^*$	slow spatial variable taking into account the variations of the flow which take place over a distance L^*
α	dimensionless wavenumber of the bottom perturbation
α_c	critical value of α
α_1	constant quantifying the difference between the actual value of α and its critical value (see (3.1))
$\beta = 0.15$	constant which takes into account the effects of the bottom slope on the sediment transport (see equation (2.11))
$\delta^* = \sqrt{2\nu^*/\omega^*}$	thickness of the viscous bottom boundary layer
$\delta = \delta^*/L^*$	viscous parameter (dimensionless thickness of the viscous bottom boundary layer)
ε	order of magnitude of the ratio between the amplitude of the bottom perturbation and δ^*, in the linear analysis
$\epsilon = \left(\sqrt{\psi_d}/\sqrt{\psi_{dc}}\right) - 1$	parameter measuring the difference between the actual mobility sediment number and its critical value
η^*	function describing the bottom elevation
$\eta = \eta^*/\delta^*$	dimensionless function describing the bottom elevation
η_0	contribution of $O(\delta Q)$ to the bottom elevation ($\eta = \delta Q \eta_0 + \varepsilon\eta_1$)
η_1	contribution of $O(\varepsilon)$ to the bottom elevation ($\eta = \delta Q \eta_0 + \varepsilon\eta_1$)

(*Continued.*)

Table 1. (*Continued.*)

ν^*	kinematic viscosity of sea water
$\psi_d = U_0^{*2}/((s-1)g^*d^*) = F_d^2$	sediment mobility number
ψ_{dc}	critical value of the sediment mobility number
ρ^*	fluid density
ρ_s^*	density of the sediment
$\tau = Q\tilde{t}$	morphodynamic temporal coordinate
$\omega^* = 2\pi/T^*$	angular frequency of the monochromatic surface wave surface

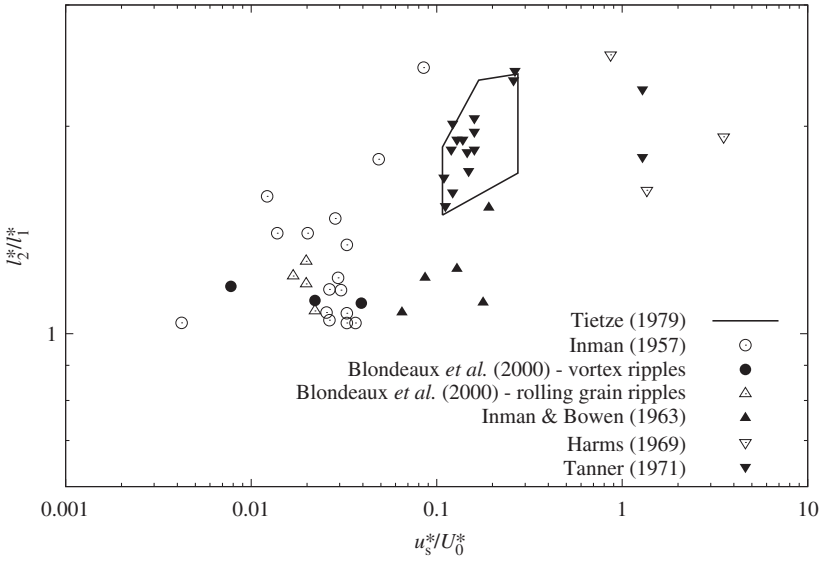

Figure 1. Ripple symmetry index plotted versus the ratio between mass-transport velocity and maximum near-bed orbital velocity. Experimental data as described in [3,4].

The mechanism through which a steady current can generate bottom forms can be understood by analysing the flow and sediment transport over a flat bed but perturbed by a small sinusoidal undulation. Assuming that the amplitude of the undulation is much smaller than the water depth, both the hydrodynamic problem and the empirical formulae usually employed to quantify the sediment transport rate can be linearized. Hence, the sediment transport rate turns out to be the sum of the sediment transport over the flat bottom plus a periodic contribution, which is induced by the bottom undulation and is not in phase with the bottom profile but characterized by a relatively small shift. Sediment continuity equation shows that the bottom perturbation amplifies when the phase shift is negative, otherwise, it decays and, in both cases, the perturbation migrates. A recent contribution to the study of ripple appearance is that of Colombini & Stocchino [23], who unified the theories of dune and ripple formation and clarified the role of ripples in the formation of dunes.

Much less is known on wave-current ripples. The interaction of a sea wave with the bottom gives always rise to an oscillatory velocity component plus a steady velocity component, the magnitude of which depends on the ratio between the height and the length of the sea wave and on the local water depth. Sometimes, the steady velocity component is not negligible when compared with the oscillating velocity component and significantly affects the ripple characteristics. Blondeaux *et al.* [4] investigated whether the steady drift has a stabilizing or a

destabilizing effect on the process of ripple formation and estimated the propagation speed of ripples and related it to the sediment flow rate. This information is of practical interest because it is common practice to evaluate the average sediment transport rate from measurements of ripple migration assuming that the sediment transport rate is related to the migration speed times the height of the ripples [24]. However, the stability analysis of Blondeaux *et al*. [4] is linear and does not provide any information on the profile of finite amplitude ripples.

The present analysis is aimed at determining ripple profile in order to relate the symmetry index of the ripples to wave and sediment characteristics. A weakly nonlinear stability analysis of a flat sandy bottom subjected to the oscillatory flow generated close to the sea bed by a propagating sea wave is presented. Second-order effects in the wave slope are retained to describe the steady drift generated by the propagation of the surface wave. Hence, the analysis of Vittori *et al*. [17] is extended.

The conditions for the decay or the amplification of a small sinusoidal perturbation of the sandy bottom were determined by Blondeaux *et al*. [4] along with the wavelength of the most unstable disturbance and its migration speed. Presently, for values of the parameters close to the marginal stability conditions, the time development of the perturbation is followed and its equilibrium profile determined. In particular, the symmetry index is computed. In §2, we formulate the model and summarize the linear solution that was determined by Blondeaux *et al*. [4]. Section 3 is devoted to describe the weakly nonlinear approach. The results of the nonlinear analysis are discussed in §4, and in §5 a discussion is presented and the main conclusions are given.

2. The linear analysis

The study of the time development of a small amplitude perturbation of the cohesionless sandy bottom forced by a monochromatic sea wave is described in [13]. As pointed out in the Introduction, Blondeaux *et al*. [4] extended the analysis by taking into account nonlinear effects in the wave steepness, but neglecting the interaction of the perturbation with itself. The analyses mentioned above are summarized hereinafter, because they are a first necessary step to develop a weakly nonlinear analysis able to determine the ripple profile, and in particular, the symmetry index of the ripples, which is the main goal of the present investigation.

In this paper, we introduce a Cartesian coordinate system with the x^*-axis lying on the average level of the bottom and pointing offshore and the y^*-axis vertical and pointing upwards. Moreover, we consider a two-dimensional gravity wave characterized by a small amplitude a^* (slowly varying in the direction of wave propagation because of viscous damping), a length L^* and a period T^*. The surface wave propagates along the x^*-axis in the negative direction (figure 2). Finally, we assume the sea bottom to be initially horizontal and flat and made up of non-cohesive sediments of uniform size d^*, density ρ_s^* and porosity p. We denote with h^* the average water depth and with ρ^*, ν^* the density and kinematic viscosity of the sea water, respectively.

Because the Reynolds number of the problem is assumed to be large, it is possible to divide the flow domain into three regions: a core region, where y^* assumes values of order h^*, a viscous boundary layer adjacent to the bottom, the thickness of which is of order $\delta^* = \sqrt{2\nu^*/\omega^*}$ ($\omega^* = 2\pi/T^*$ is the angular frequency of the sea wave) and a surface layer. Because we are interested in the interaction between the fluid and the sediment motions, we focus our attention on the bottom boundary layer. The flow induced by wave propagation is usually determined assuming that the wave slope is much smaller than one

$$a = \frac{a^*}{L^*} \ll 1. \tag{2.1}$$

However, it turns out that

$$\delta = \frac{\delta^*}{L^*} = \frac{a^*}{L^*} \frac{2}{\sinh(2\pi h^*/L^*)Re} \ll 1, \tag{2.2}$$

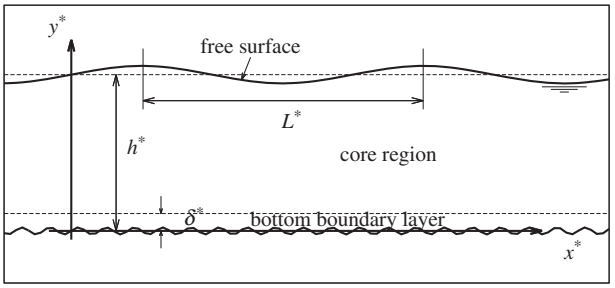

Figure 2. Sketch of the problem.

where the Reynolds number is defined by

$$Re = \frac{U_0^* \delta^*}{\nu^*}, \tag{2.3}$$

where $U_0^* = a^*\omega^*/\sinh(2\pi h^*/L^*)$ is the amplitude of the irrotational velocity oscillations close to the bottom and δ^* being the thickness of the viscous bottom boundary layer, previously introduced. Therefore, the dimensionless velocity components $(u, v) = (u^*, v^*)/U_0^*$ in the bottom boundary layer can be expanded using δ as a small parameter

$$(u, v) = (u_{00}, v_{00}) + \delta(u_{10}, v_{10}) + O(\delta^2). \tag{2.4}$$

Indeed, if δ is replaced by $2a/[Re\sinh(2\pi h^*/L^*)]$ in (2.4), the usual expansion of the velocity field in terms of the wave steepness is recovered. The solution of the hydrodynamic problem is expanded using δ instead of the more usual parameter a, because the viscous parameter δ would appear anyway in the hydrodynamic problem, owing to the relevance of the viscous effects in the bottom boundary layer. The use of the expansion (2.4) avoids the introduction of two unnecessary independent parameters much smaller than one.

The form of $u_{00}, v_{00}, u_{10}, v_{10}$ as functions of $t = \omega^* t^*$ and $(\tilde{x}, \tilde{y}) = (x^*, y^*)/\delta^*$ can be found in [25] or alternatively in [26]

$$u_{00} = \hat{u}_{00}(\tilde{y})\,\mathrm{e}^{\mathrm{i}(t+2\pi\delta\tilde{x})} + \text{c.c.}, \quad v_{00} = 0 \tag{2.5}$$

and

$$u_{10} = [\bar{u}_{10}(\tilde{y}) + \hat{u}_{10}(\tilde{y})\,\mathrm{e}^{\mathrm{i}(t+2\pi\delta\tilde{x})}] + \text{c.c.}, \quad v_{10} = \hat{v}_{10}\,\mathrm{e}^{\mathrm{i}(t+2\pi\delta\tilde{x})} + \text{c.c.}, \tag{2.6}$$

where c.c. indicates the complex conjugate of the previous complex quantity and

$$\hat{u}_{00} = -\frac{1}{2}[1 - \mathrm{e}^{-(1+\mathrm{i})\tilde{y}}] \tag{2.7}$$

$$\bar{u}_{10} = -\frac{\pi Re}{4}\left\{\frac{3}{2} + \frac{1}{2}\mathrm{e}^{-2\tilde{y}} - \mathrm{e}^{-(1-\mathrm{i})\tilde{y}}[2 + \mathrm{i} + (1-\mathrm{i})\tilde{y}]\right\} \tag{2.8}$$

$$\hat{u}_{10} = -\frac{\pi Re}{4}\left\{\frac{3}{2\cosh(4\pi h^*/L^*) - \sinh(4\pi h^*/L^*)/\tanh(2\pi h^*/L^*)} + \mathrm{e}^{-(1+\mathrm{i})\tilde{y}}[1 - (1+\mathrm{i})\tilde{y}] - \mathrm{e}^{-\sqrt{2}(1+\mathrm{i})\tilde{y}}\left[1 + \frac{3}{2\cosh(4\pi h^*/L^*) - \sinh(4\pi h^*/L^*)/\tanh(2\pi h^*/L^*)}\right]\right\} \tag{2.9}$$

and

$$\hat{v}_{10} = \pi\mathrm{i}\left[\tilde{y} + \frac{1}{1+\mathrm{i}}(\mathrm{e}^{-(1+\mathrm{i})\tilde{y}} - 1)\right]. \tag{2.10}$$

The flow field is characterized by the presence of a steady velocity component $\bar{u}_{10}$, which arises because a time average shear stress should be present to balance the mean momentum flux owing to the wave velocity fluctuations and the mean pressure field [25].

To verify that the use of the expansion (2.4) does not introduce any limitation on the values of the Reynolds number Re that can be considered, let us follow [27] and evaluate the ratio

between the order of magnitude of the second term on the right-hand side of (2.4) and the order of magnitude of the first term on the right-hand side of (2.4). This ratio is equal to the Ursell number and does not depend on the Reynolds number Re. It follows that Re can assume any value as long as the parameter $a = \delta\, Re\, \sinh[2\pi h^*/L^*]$ is smaller than one, and the flow regime is laminar. Indeed, the analysis is based on the Navier–Stokes equation, and turbulence stresses are not considered. In other words, Re can assume any value up to the critical value Re_c for transition to turbulence, which falls between 500 and 600.

The reader should note that the first index in (2.4) indicates the order of the parameter that measures the wave steepness, whereas the second index indicates the order of the parameter that measures the steepness of the bottom forms, which are considered in the following.

Because the sediment is transported by the fluid motion, the propagation of a surface wave induces changes of the plane bottom configuration. The time development of the bottom profile is provided by sediment continuity equation together with a relationship between the sediment flow rate per unit width q^* and the flow field. Here, we employ the same empirical formulation for q^* as that of Blondeaux *et al*. [4], even though it is possible to modify the analysis using other sediment transport predictors. Using dimensionless variables, we can write

$$q = \frac{q^*}{\sqrt{(\rho_s^*/\rho^* - 1) g^* d^{*3}}} = \hat{a} \left| \frac{2}{R_d} V - \frac{\beta}{\psi_d} \frac{\partial \eta}{\partial x} \right|^{b-1} \left(\frac{2}{R_d} V - \frac{\beta}{\psi_d} \frac{\partial \eta}{\partial x} \right), \tag{2.11}$$

where $y^* = \eta^*(x,t)$ describes the bed elevation, and V^* is the fluid velocity parallel to the bottom at $y^* = \eta^* + d^*/2$. Moreover, in (2.11), $\tilde{y} = \eta(x,t)$ describes the dimensionless bed elevation, $V = V^*/U_0^*$, $d = d^*/\delta^*$ and the sediment mobility number ψ_d, the particle Reynolds number R_d and the relative density s of the sediments are defined by

$$\psi_d = \frac{U_0^{*2}}{(s-1) g^* d^*}, \quad R_d = \frac{U_0^* d^*}{\nu^*} \quad \text{and} \quad s = \frac{\rho_s^*}{\rho^*}. \tag{2.12}$$

The constant β appearing in (2.11) takes into account the effects of the bottom slope on the sediment transport and is fixed equal to 0.15 as in [13]. The values of $\hat{a}$ and b were estimated in the relevant range of the parameters by requiring that relationship (2.11) should match the empirical formula proposed by Grass & Ayoub [28]. The reader should note that ψ_d is equal to F_d^2, i.e. to the square of the particle Froude number defined by [13]. It turns out that

$$\hat{a} = 1.23 \frac{s-1}{s} \psi_d^{3.36} R_d^{1.83}, \quad b = 4.28. \tag{2.13}$$

Alternatively, it is convenient to write q in the form

$$q = Q\tilde{q} = Q \left| \frac{2Re}{R_d} V - \frac{\beta Re}{\psi_d} \frac{\partial \eta}{\partial x} \right|^{b-1} \left(\frac{2Re}{R_d} V - \frac{\beta Re}{\psi_d} \frac{\partial \eta}{\partial x} \right), \tag{2.14}$$

where

$$Q = \frac{\hat{a} R_d}{2(1-p)\sqrt{\psi_d} Re^b}. \tag{2.15}$$

In this way, the function $\tilde{q}$ is of order one, and the quantity Q is much smaller than one (here p is the porosity of the sea bed). The dimensionless form of sediment continuity equation reads

$$\frac{\partial \eta}{\partial \tilde{t}} = -Q \left[\frac{\partial \tilde{q}}{\partial \tilde{x}} + 2\pi\delta \frac{\partial \tilde{q}}{\partial \tilde{t}} \right], \tag{2.16}$$

where the variable $\tilde{t} = t + 2\pi\delta\tilde{x}$ is introduced to reduce the amount of algebra that is necessary to find the solution. The sediment balance equation (2.16) simply states that erosion and deposition processes are due to the spatial variations of the sediment transport rate. These variations are induced by the bottom undulation (first term on the right-hand side of (2.16)) and by the propagation of the surface wave (second term on the right-hand side of (2.16)). However, the latter variations are much smaller than the former because they take place on a spatial scale L^* that is much longer than the boundary layer thickness $O(\delta^*)$. Because of the small values assumed

by the parameter Q, equation (2.16) suggests that, even when $\partial\tilde{q}/\partial\tilde{x}$ is of order 1, the bottom changes are either quite small, i.e. of $O(Q)$, or take place on a slow morphological time scale $\tau = Q\tilde{t}$. Therefore, the flow induced by the propagation of the surface wave can be evaluated by considering a parametrically varying bottom profile, if terms of order Q are neglected. Because the sea wave, which propagates over a flat bottom, is characterized by no spatial dependence on the fast variable $\tilde{x}$ but only on the slow variable $x = \delta^*\tilde{x}/L^*$, the bottom variations turn out to be of order δQ. At the leading order of approximation, it is thus possible to write

$$\eta = \delta Q \eta_0. \tag{2.17}$$

Because sediment transport at the bottom of a sea wave is observed to be in the direction of wave propagation in front of the crests and in the opposite direction in front of the troughs, it appears that sediments are piled up behind wave troughs while they are swept away behind the crests, thus generating a wavy bottom. No sand wave with the same period and wavelength of the surface water wave has ever been observed in the field because of the slow spatial variations of q^* and the high frequency of water waves. Indeed, the order of magnitude of the amplitude of this bedform can be estimated by using sediment continuity equation [24] and it turns out to be

$$\frac{\bar{q}^* T^*}{L^*},$$

where $\bar{q}^*$ is the sediment transport rate averaged over half a cycle. Whatever formula is used to compute q^*, the amplitude of the sandy wave turns out to be much smaller than the size of the sand grains.

It follows that, neglecting terms of order δQ, the velocity field provided by (2.4)–(2.10) describes the flow even over a cohesionless movable bottom. Then, from sediment continuity equation, it follows that

$$\eta_0 = -2\pi \left| \frac{2Re}{R_d} u_{00} \right|^{(b-1)}_{\tilde{y}=\eta+d/2} \left(\frac{2Re}{R_d} u_{00} \right)_{\tilde{y}=\eta+d/2}. \tag{2.18}$$

Equations (2.17) and (2.18) describe an undulation of the bottom of length L^* equal to that of the sea wave and an amplitude of order $\delta^{*2}Q/L^*$, which is quite hard to observe in the field because of its smallness.

Now, we want to investigate the stability of this bottom profile. Hence, we superimpose a perturbation of small amplitude ε to the basic bottom profile

$$\eta = \delta Q \eta_0 + \varepsilon \eta_1(\tilde{x}, \tilde{t}). \tag{2.19}$$

Actual values of Q and δ are of order 10^{-3} and 10^{-5}, respectively. It follows that it is possible and reasonable to consider situations such that

$$\delta Q \ll \varepsilon \ll 1. \tag{2.20}$$

In other words, we consider amplitudes of the bottom perturbation that are much smaller than δ^*, but larger than the amplitude $(\delta Q)\delta^*$ of the sandy wave produced by the propagation of the sea surface wave over the cohesionless bottom. Because of the assumption of a small amplitude perturbation, it is feasible to perform a normal mode analysis and to consider a generic component of the bottom perturbation in the form

$$\varepsilon \eta_1(\tilde{x}, \tilde{t}) = \varepsilon C_1(\tilde{t})\, \mathrm{e}^{\mathrm{i}\alpha\tilde{x}} + \text{c.c.}, \tag{2.21}$$

where α is the dimensionless wavenumber of the bottom undulation. A careful analysis of the order of magnitude of the different terms of momentum and continuity flow equations and Exner equation shows that the flow generated by the propagation of the sea wave over the perturbed bottom can be written in the form

$$(u, v) = (u_{00}, v_{00}) + \delta(u_{10}, v_{10}) + \varepsilon\{C_1(\tilde{t})[(\hat{u}_{01}, \hat{v}_{01}) + \delta(\hat{u}_{11}, \hat{v}_{11})]\, \mathrm{e}^{\mathrm{i}\alpha\tilde{x}} + \text{c.c.}\} + O(\delta^2, \varepsilon^2, Q). \tag{2.22}$$

The functions $\hat{u}_{01}, \hat{v}_{01}, \hat{u}_{11}, \hat{v}_{11}$ are periodic in the fast temporal coordinate $\tilde{t}$ (measuring the variations of the velocity field at the wave time scale), and thus they can be written as Fourier series

$$(\hat{u}_{n1}, \hat{v}_{n1}) = \sum_{m=-\infty}^{\infty} (\hat{u}_{n1}^{(m)}(\tilde{y}), \hat{v}_{n1}^{(m)}(\tilde{y}))\, \mathrm{e}^{\mathrm{i}m\tilde{t}} \quad \text{for } n = 0, 1. \tag{2.23}$$

The expansion (2.23) shows the existence of spatially periodic oscillating cells with a non-vanishing time average. If (2.22) and (2.23) are plugged into momentum and continuity equations and terms of order ε^0 are considered, the solutions of the hydrodynamic problems, which are found by considering terms of order δ^0 and terms of order δ, are obtained by straightforward means and $u_{00}, v_{00}, u_{10}, v_{10}$ are provided by (2.5)–(2.10). The terms of order $\varepsilon\delta^0$ and $\varepsilon\delta$ are considered, separately. The ordinary differential equations that provide the functions $\hat{u}_{n1}^{(m)}(\tilde{y})$, $\hat{v}_{n1}^{(m)}(\tilde{y})$ are solved numerically by means of a Runge–Kutta approach of second order and using a shooting method to force the boundary conditions at the bottom and far from it. Details of the procedure can be found, among others, in [17].

Once the flow field at order ε is determined, the sediment transport rate is quantified by writing it in the form

$$\tilde{q} = (\tilde{q}_{00} + \delta\tilde{q}_{10}) + [\varepsilon C_1(\tilde{t})(\tilde{q}_{01} + \delta\tilde{q}_{11})\, \mathrm{e}^{\mathrm{i}\alpha\tilde{x}} + \text{c.c.}] + O(\delta^2, \varepsilon^2, Q). \tag{2.24}$$

Expressions for the variables $\tilde{q}_{00}, \tilde{q}_{10}, \tilde{q}_{01}, \tilde{q}_{11}$ are given in [4]. Moreover, the analysis of Blondeaux [13] suggests that the amplitude of the bottom perturbation depends on two time coordinates: a fast time coordinate $\tilde{t}$ and a slow, morphodynamic time coordinate $\tau = Q\tilde{t}$

$$C_1(\tilde{t}) = \mathcal{C}(\tau)[1 + Q\mathcal{C}_1^{(1)}(\tilde{t}) + O(Q^2)]. \tag{2.25}$$

At order εQ, sediment balance leads to

$$\mathcal{C}\frac{\mathrm{d}\mathcal{C}_1^{(1)}}{\mathrm{d}\tilde{t}} + \frac{\mathrm{d}\mathcal{C}}{\mathrm{d}\tau} = -\left[\mathrm{i}\alpha(\tilde{q}_{01} + \delta\tilde{q}_{11}) + 2\pi\delta\frac{\mathrm{d}\tilde{q}_{01}}{\mathrm{d}\tilde{t}}\right]\mathcal{C}, \tag{2.26}$$

which gives rise to

$$\frac{\mathrm{d}\mathcal{C}}{\mathrm{d}\tau} = \left[-\frac{\mathrm{d}\mathcal{C}_1^{(1)}}{\mathrm{d}\tilde{t}} + G(\tilde{t})\right]\mathcal{C}. \tag{2.27}$$

The function $G(\tilde{t})$ is provided by

$$G(\tilde{t}) = -\mathrm{i}\alpha\tilde{q}_{01} - \delta\left[\mathrm{i}\alpha\tilde{q}_{11} + 2\pi\frac{\mathrm{d}\tilde{q}_{01}}{\mathrm{d}\tilde{t}}\right] = \bar{G} + \hat{G}(\tilde{t}), \tag{2.28}$$

and it appears to be the sum of a periodic function $\hat{G}(\tilde{t})$ with a vanishing time average and a constant value $\bar{G}$. It follows that two equations are obtained by the sediment balance at order εQ

$$\frac{\mathrm{d}\mathcal{C}_1^{(1)}}{\mathrm{d}\tilde{t}} = \hat{G}(\tilde{t}) \tag{2.29}$$

and

$$\frac{\mathrm{d}\mathcal{C}}{\mathrm{d}\tau} = \bar{G}\mathcal{C}(\tau). \tag{2.30}$$

The function $\mathcal{C}_1^{(1)}(\tilde{t})$ is provided by $\mathcal{C}_1^{(1)} = \int \hat{G}(\tilde{t})\, \mathrm{d}\tilde{t}$ and it describes the small periodic variations of the perturbation profile during a wave cycle. More precisely, the real part describes oscillations of the amplitude of the bottom perturbation, whereas the imaginary part controls the small longitudinal oscillations of the ripple profile around its average position. The growth and migration of the perturbation/ripple are controlled by $\bar{G} = \bar{G}_0 + \delta\bar{G}_1$ with $\bar{G}_0 = \overline{-\mathrm{i}\alpha\tilde{q}_{01}}$ and $\bar{G}_1 = \overline{-\mathrm{i}\alpha\tilde{q}_{11}}$. More precisely, the real part $\bar{G}_\mathrm{r} = \bar{G}_{0\mathrm{r}} + \delta\bar{G}_{1\mathrm{r}}$ of $\bar{G}$ controls the amplification/decay

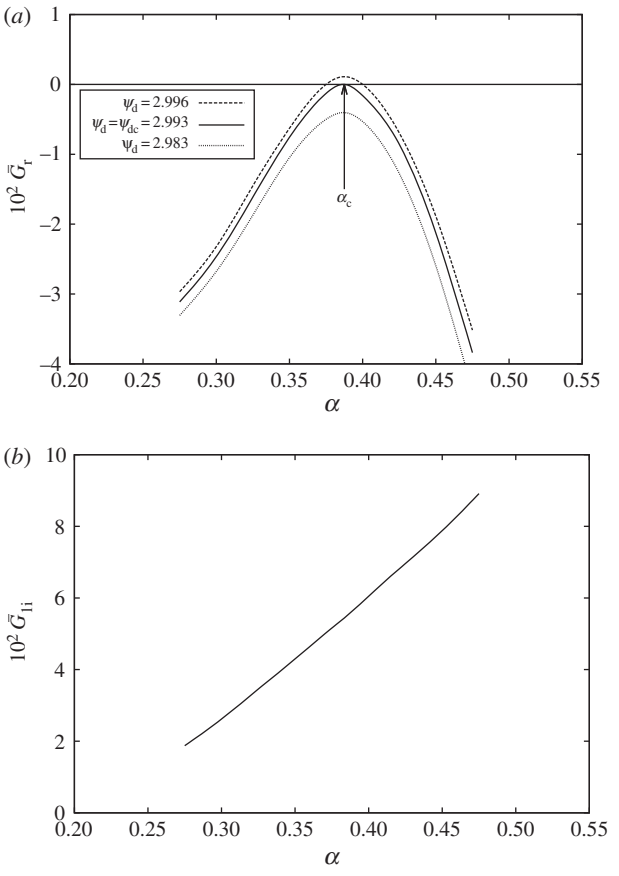

Figure 3. (*a*) Real part of $\bar{G}$ and (*b*) imaginary part of $\bar{G}_1$ plotted versus α for different values of ψ_d and $Re = 35$, $R_d = 10$. The values of the imaginary part of $\bar{G}_1$ do not depend on ψ_d.

of the perturbation and the imaginary part $\bar{G}_i = \delta\bar{G}_{1i}$ controls the migration ($\bar{G}_{0i}$ vanishes because of the symmetry of the problem at the leading order of approximation). Indeed, (2.30) shows that

$$\mathcal{C}(\tau) = \mathcal{C}_0 \exp(\bar{G}\tau) \tag{2.31}$$

and (2.21) leads to

$$\varepsilon\eta_1(\tilde{x}, t) = \varepsilon C_0 \exp[(\bar{G}_{0r} + \delta\bar{G}_{1r})\tau] \exp\left[\mathrm{i}\alpha\left(\tilde{x} + \frac{\delta\bar{G}_{1i}}{\alpha}\tau\right)\right] + \text{c.c.} \tag{2.32}$$

The value of $\bar{G}_0 = \bar{G}_{0r}$ is identical to the amplification rate found by Blondeaux [13], whereas $\bar{G}_i = \delta\bar{G}_{1i}$ was determined by Blondeaux *et al*. [4] and is due to second-order effects in the wave slope.

The results of the linear analysis are discussed in Blondeaux *et al*. [4], where the interested reader can also find an exhaustive discussion of the influence of second order terms in the wave slope on the stability of the sea bottom. Herein, let us show only an example of the results (figure 3). The plot of $\bar{G}_{0r}$ (figure 3*a*) shows the existence of a critical value ψ_{dc} of ψ such that for ψ smaller than ψ_{dc}, bottom perturbations decay for any value of the wavenumber α. On the other hand, for ψ_d larger than ψ_{dc}, bottom perturbations characterized by values of α falling in a restricted range around the critical value α_c experience an average amplification within a cycle. The results of figure 3*b* indicate that the growth of bottom perturbations takes place simultaneously with their migration in the onshore direction. Indeed, the imaginary part of $\bar{G}$

turns out to be positive whatever value of α is considered (we remind the reader that the x-axis points offshore).

As pointed out in the Introduction, the bottom perturbation grows and gives rise to bedforms, because the interaction of the oscillatory flow induced by the surface waves with the bottom undulation gives rise to recirculating cells, which tend to move the sediment from the troughs towards the crests of the bottom undulation. The tendency of the sediment to move towards the crests is opposed by gravity effect, and the ripple wavelength is the result of a balance between these two effects. If terms of $O(\delta)$ are neglected, the steady recirculating cells are symmetric with respect to the crests and the troughs of the ripple profile. Hence, because of this symmetry, the bottom forms do not migrate. The terms of $O(\delta)$ break this symmetry, and the ripples migrate with a speed that is of $O(\delta)$ and they move in the direction of the steady streaming.

3. The weakly nonlinear stability analysis

The analysis, which is described in §2, neglects the nonlinear effects related to the perturbation amplitude. It follows that the bottom profile predicted by the stability analysis turns out to be sinusoidal and its amplitude is defined but for an arbitrary multiplying factor. To mimic the process, which shapes the bottom profile giving rise to bottom forms characterized by crests sharper than the troughs and up-current slopes smaller than the down-current slopes, it is necessary to consider the interaction of the bottom perturbation with itself.

When the presence of the steady drift in the direction of wave propagation is neglected by assuming vanishing values of δ, a stability analysis which takes into account weakly nonlinear effects was carried out by Vittori & Blondeaux [17]. Their results describe the actual height, wavelength and profile of the ripple as a function of the parameters for a pure oscillatory flow. In particular, the obtained results show that the ripple profile is symmetric with respect to ripple crests and troughs even though the crests are sharper than the troughs. If δ is different from zero but keeps small, an analysis similar to that of Vittori & Blondeaux [17] can be performed.

The linear analysis allows us to determine the marginal stability curve that divides the (α, ψ_d)-plane into two regions. One where the flat bottom is stable and the other where ripples tend to appear. Figure 4 shows an example of the marginal stability curve for $Re = 30$ and $R_d = 10$. This curve is characterized by a minimum that is located at $(\alpha_c, \psi_{dc}) \cong (0.42, 2.87)$. It follows that, for $Re = 30, R_d = 10$ and ψ_d smaller than 2.87, any random perturbation of small amplitude decays and the flat bottom turns out to be stable. On the other hand, if ψ_d is larger than 2.87, the harmonic spatial components of a random perturbation, which are characterized by dimensionless wavenumbers α much larger or much smaller than 0.42, decay. However, the harmonic components characterized by dimensionless wavenumbers falling in a restricted range around $\alpha = 0.42$ tend to grow and to generate ripples.

These values of the dimensionless parameters correspond to laboratory experiments made in a wave channel where the water depth is 33 cm and waves of height and period equal to 2 cm and 1.5 s, respectively, are generated. A critical value of the mobility number equal to 2.87 is found for nylon pellets characterized by a mean size equal to 0.25 mm and a relative density of 1.27. It follows that rolling-grain ripples do not form when the bottom material is heavier and they appear for lighter materials. Moreover, the ripples that appear should have a wavelength of about 1 cm. The interested reader can verify that these values of the parameters are similar to those of the experiments described in [29].

To determine the time development of the growing components, let us fix the values of Re and R_d and let us consider mobility numbers ψ_d and perturbation wavenumbers α such that

$$\sqrt{\psi_d} = \sqrt{\psi_{dc}}(1 + \epsilon); \quad \alpha = \alpha_c + \epsilon\alpha_1. \tag{3.1}$$

Herein, ϵ is a small parameter denoting the difference between the actual mobility number ψ_d and its critical value ψ_{dc}, α_c is the critical wavenumber for fixed values of Re and R_d, whereas α_1 is an arbitrary parameter of order one, which allows perturbations with wavenumbers slightly different from α_c to be investigated. Relationships (3.1) imply that the bottom perturbation is

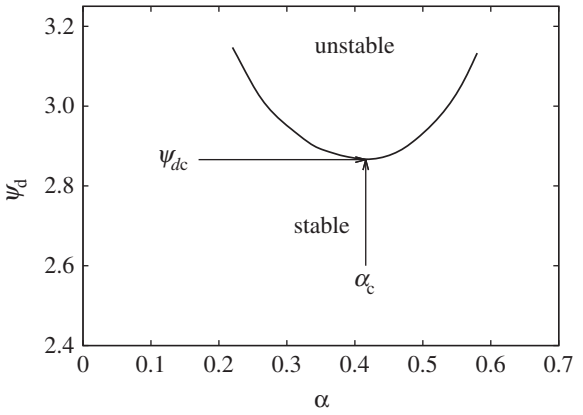

Figure 4. Marginal stability curve in the plane (α, ψ_d) for $Re = 30$, $R_d = 10$.

examined in the weakly nonlinear regime, allowing its wavenumber α to be 'slightly' perturbed with respect to the critical value α_c. From the results of the linear analysis, it can be verified that in the neighbourhood of the critical condition defined by (3.1), the amplification rate of an initially infinitesimal bottom perturbation is of order ϵ. For this reason, in the weakly nonlinear regime, the process is described in terms of the fast time coordinate $\tilde{t}$ characteristic of the wave field as well as of a slow time coordinate $\mathcal{T}$ characteristic of the bottom time development

$$\mathcal{T} = \epsilon Q \tilde{t} \tag{3.2}$$

that implies

$$\frac{\partial}{\partial \tilde{t}} \to \frac{\partial}{\partial \tilde{t}} + \epsilon Q \frac{\partial}{\partial \mathcal{T}}. \tag{3.3}$$

In order to derive the order of magnitude of the amplitude of the perturbation, the following argument holds: nonlinearity gives rise to interactions of the fundamental with itself and with the basic flow, which lead to the generation of higher harmonics. Following the above cascade process, one finds that the fundamental is reproduced at third order and secular terms are generated. In order to prevent their occurrence the 'slow' time dependence of the amplitude A of the fundamental must also be forced to produce a contribution at third order. In other words, $\epsilon(\partial A/\partial T)$ must balance A^3, which occurs provided $O(A) = O(\epsilon^{1/2})$. Then, we expand the bottom configuration and the flow field in the form

$$\begin{aligned}\eta(\tilde{x}, \tilde{t}, \mathcal{T}) = \epsilon^{1/2}[A(\mathcal{T})C_1(\tilde{t})\,\mathrm{e}^{\mathrm{i}\alpha\tilde{x}} + \text{c.c.}] + \epsilon[A^2(\mathcal{T})C_2(\tilde{t})\,\mathrm{e}^{2\mathrm{i}\alpha\tilde{x}} + \text{c.c.}] + \epsilon^{3/2}[A(\mathcal{T})|A(\mathcal{T})|^2 C_3(\tilde{t})\,\mathrm{e}^{\mathrm{i}\alpha\tilde{x}} \\ + \text{c.c.} + \text{other terms, not relevant for the present analysis}] + O(\epsilon^2)\end{aligned} \tag{3.4}$$

and

$$\begin{aligned}&(u(\tilde{x}, \tilde{y}, \tilde{t}, T), v(\tilde{x}, \tilde{y}, \tilde{t}, \mathcal{T})) \\ &= (u_0(\tilde{y}, \tilde{t},), v_0(\tilde{y}, \tilde{t})) + \epsilon^{1/2}[A(\mathcal{T})C_1(\tilde{t})(\hat{u}_1(\tilde{y}, \tilde{t}), \hat{v}_1(\tilde{y}, \tilde{t}))\,\mathrm{e}^{\mathrm{i}\alpha\tilde{x}} + \text{c.c.}] \\ &\quad + \epsilon[|A(\mathcal{T})|^2|C_1(\tilde{t})|^2(\hat{u}_2^{(1)}(\tilde{y}, \tilde{t}), \hat{v}_2^{(1)}(\tilde{y}, \tilde{t})) \\ &\quad + A^2(\mathcal{T})(C_1^2(\tilde{t})(\hat{u}_2^{(2)}(\tilde{y}, \tilde{t}), \hat{v}_2^{(2)}(\tilde{y}, \tilde{t})) + C_2(\tilde{t})(\hat{u}_2^{(3)}(\tilde{y}, \tilde{t}), \hat{v}_2^{(3)}(\tilde{y}, \tilde{t}))\,\mathrm{e}^{2\mathrm{i}\alpha\tilde{x}} + \text{c.c.}] \\ &\quad \times \epsilon^{3/2}[A(\mathcal{T})|A(\mathcal{T})|^2(C_1(\tilde{t})|C_1(\tilde{t})|^2(\hat{u}_3^{(1)}(\tilde{y}, \tilde{t}), \hat{v}_3^{(1)}(\tilde{y}, \tilde{t})) + C_3(\tilde{t})(\hat{u}_3^{(3)}(\tilde{y}, \tilde{t}), \hat{v}_3^{(3)}(\tilde{y}, \tilde{t}))\,\mathrm{e}^{\mathrm{i}\alpha\tilde{x}} \\ &\quad + \text{c.c.} + \text{other terms, not relevant for the present analysis}] + O(\epsilon^2),\end{aligned} \tag{3.5}$$

where $A(\mathcal{T})$ represents the amplitude of the fundamental component of the bottom perturbation (averaged over a wave cycle), which evolves on the slow time coordinate $\mathcal{T}$, and $\hat{u}_1, \hat{v}_1, u_2^{(0)}, v_2^{(0)}, \hat{u}_2^{(3)}, \ldots$ are functions of $\tilde{y}$ and $\tilde{t}$ and depend on the parameters h, Re.

The reader can verify that in (3.5) different contributions appear: (i) the oscillatory flow (u_0, v_0) within the boundary layer under a monochromatic surface wave propagating over a flat bottom, (ii) a correction of order $\epsilon^{1/2}$ that is due to a bottom undulation of small amplitude, and (iii) a term of order ϵ that is due to the nonlinear interaction of the flow generated by the bottom undulation of order $\epsilon^{1/2}$ with itself. This interaction leads to the appearance of a contribution that does not depend on $\tilde{x}$ and a contribution that is proportional to $e^{2i\alpha\tilde{x}}$. The divergence of the sediment transport generated by the latter gives rise to a bottom undulation that, in turn, linearly generates a correction of order ϵ of the flow field, (iv) two terms of order $\epsilon^{3/2}$ that are generated by nonlinear effects and by the presence of a bottom undulation of order $\epsilon^{3/2}$, respectively. In (3.4) and (3.5), only these terms, which are proportional to $e^{i\alpha\tilde{x}}$, are explicitly shown, because the other terms of order $\epsilon^{3/2}$ are not relevant to the present analysis.

The terms appearing in (3.5) can be found by splitting them in a contribution of order δ^0 and a contribution of order δ:

$$\left.\begin{aligned} &(u_0, v_0) = (u_{00}, 0) + \delta(u_{10}, v_{10}), \quad (\hat{u}_1, \hat{v}_1) = (\hat{u}_{01}, \hat{v}_{01}) + \delta(\hat{u}_{11}, \hat{v}_{11}) \\ &(\hat{u}_2^{(1)}, \hat{v}_2^{(1)}) = (\hat{u}_{02}^{(1)}, \hat{v}_{02}^{(1)}) + \delta(\hat{u}_{12}^{(1)}, \hat{v}_{12}^{(1)}), \quad (\hat{u}_2^{(2)}, \hat{v}_2^{(2)}) = (\hat{u}_{02}^{(2)}, \hat{v}_{02}^{(2)}) + \delta(\hat{u}_{12}^{(2)}, \hat{v}_{12}^{(2)}) \\ \text{and} \quad &(\hat{u}_2^{(3)}, \hat{v}_2^{(3)}) = (\hat{u}_{02}^{(3)}, \hat{v}_{02}^{(3)}) + \delta(\hat{u}_{12}^{(3)}, \hat{v}_{12}^{(3)}). \end{aligned}\right\} \tag{3.6}$$

The functions $\hat{u}_{jk}^{(i)}$, $\hat{v}_{jk}^{(i)}$ appearing in (3.6) can be determined by solving the ordinary differential equations obtained by plugging (3.5) and (3.6) into continuity and momentum equations and collecting terms of equal order in $\varepsilon^{(1/2)}$ and δ. The solution is found numerically by means of a Runge–Kutta method of second order and a shooting procedure. Once the flow is known, the sediment balance can be considered at the different order of approximation. Below, we present further details.

The $O(\epsilon^{1/2})$ sediment continuity equation.

The value of $C_1(\tilde{t})$ is already known and provided by (2.25). Moreover, the function $\mathcal{C}$ turns out to be a constant, which can be assumed to be equal to one, without loss of generality. The latter conclusion is based on the observation that the physical parameters of the problem fall within a neighbourhood of the critical conditions or, from a mathematical point of view, on the assumptions (3.1). It follows that the growth/decay of the ripples is provided only by $A(\mathcal{T})$, which is not known at this order of approximation.

The $O(\epsilon)$ sediment continuity equation.

As before, we expand C_2 in the form

$$C_2(\tilde{t}) = C_2^{(0)}(\tilde{t}) + QC_2^{(1)}(\tilde{t}) + O(Q^2). \tag{3.7}$$

Making use of (2.14) and (2.16), at order ϵQ, we find

$$\frac{dC_2^{(1)}(\tilde{t})}{d\tilde{t}} = [f(\tilde{t}) + C_2^{(0)} g(\tilde{t})], \tag{3.8}$$

where the functions $f(\tilde{t})$ and $g(\tilde{t})$, which can be found by means of long and tedious but straightforward algebra, are periodic functions of time. The time derivative of $C_2^{(1)}$ is thus given by the sum of two contributions. The first contribution $(f(\tilde{t}))$ is related to the flow field arising from the nonlinearity of the problem. The second contribution $(C_2^{(0)} g(\tilde{t}))$ is related to the flow induced by the second harmonic component of the bottom profile. Because $C_2^{(1)}$ should remain bounded, the time average over a period of the right-hand side of (3.8) should vanish. This

condition determines the value of the constant $C_2^{(0)}$, i.e. the amplitude of the bottom second spatial harmonic component

$$C_2^{(0)} = -\frac{\int_0^{2\pi} f(\tilde{t})\,\mathrm{d}\tilde{t}}{\int_0^{2\pi} g(\tilde{t})\,\mathrm{d}\tilde{t}}. \tag{3.9}$$

From a physical point of view relationship (3.9) forces the amplitude of the bottom second harmonic in such a way that the gravity component along the bed profile at second order exactly balances the second-order component of the shear stress acting on the sediment caused by the steady streaming associated with both $(\hat{u}_2^{(2)}, v_2^{(2)})$ and $(\hat{u}_2^{(3)}, v_2^{(3)})$. Then, from (3.8) and using (3.9), we find

$$C_2^{(1)} = \int_{\tilde{t}_0}^{\tilde{t}} [f(\tilde{t}) + C_2^{(0)} g(\tilde{t})\,\mathrm{d}\tilde{t}]\,\mathrm{d}\tilde{t}. \tag{3.10}$$

Even though the functions f and g differ from those given in [17] only for terms of $O(\delta)$, the value of the constant $C_2^{(0)}$ that comes from (3.9) gives rise to ripple profiles that show qualitative differences from those described in [17]. If terms of $O(\delta)$ are neglected in (3.9), $C_2^{(0)}$ turns out to be real and thus the second spatial harmonic is in phase with the first one, whatever value of $A(\mathcal{T})$. Hence, the ripple profile has the crests that are sharper than the troughs ($C_2^{(0)}$ is positive) but it is still symmetric with respect to the crests and the troughs. On the other hand, if $O(\delta)$ terms are retained in (3.9), $C_2^{(0)}$ has an imaginary part, and thus the ripple profile is no longer symmetric.

The $O(\epsilon^{3/2})$ continuity equation.

Let us finally come to sediment continuity at $O(\epsilon^{3/2})$. In order to avoid a secular growth of the bottom perturbation, a solvability condition should be forced. This condition leads to an equation for the amplitude $A(\mathcal{T})$, which is of Landau–Stuart type

$$\frac{\mathrm{d}A}{\mathrm{d}\mathcal{T}} = a_1 A + a_2 A^2 A^+, \tag{3.11}$$

where the coefficients a_1 and a_2 differ from those determined by Vittori & Blondeaux [17] only for terms of $O(\delta)$ and A^+ denotes the complex conjugate of A. If terms of $O(\delta)$ and Q are neglected, both a_1 and a_2 turn out to be real. On the other hand, a_1 and a_2 turn out to be complex if terms of $O(\delta)$ are considered. These results would suggest to investigate the time development of a perturbation characterized by a narrow spectrum of wavenumbers around α_c. In this case, the analysis would lead to a Ginzburg–Landau equation instead of the Landau–Stuart equation (3.11). Taking into account that the presence of a narrow spectrum of unstable wavenumbers causes only a slow spatial modulation of the amplitude of the ripples, the Landau–Stuart equation is considered appropriate for the purposes of the present analysis.

The time development of the amplitude of the bottom forms, provided by (3.11), is

$$|A(\mathcal{T})| = \sqrt{\frac{\mathrm{real}(a_1)}{\exp[-2\,\mathrm{real}(a_1)\mathcal{T}] - \mathrm{real}(a_2)}}. \tag{3.12}$$

When the amplitude of the perturbation is small and nonlinear terms can be neglected in (3.11), the exponential growth of the perturbation is recovered, if ψ_d is larger than ψ_{dc}. Indeed, the steady recirculating cells, generated by the linear interaction between the basic oscillatory flow with the bottom undulation, tend to move the sediment from the troughs to the crests of the bottom undulation and to originate ripples. The wavelength of the ripples is determined by a balance between the destabilizing effects and the stabilizing effects owing to gravity acceleration. As soon as the amplitude assumes significant values, the nonlinear effects modify the shape and the strength of the recirculating cells. From a mathematical point of view, the term $a_2 A^2 A^+$ appearing

in (3.11) slows down the growth until an equilibrium is attained. The equilibrium amplitude $|A_e|$ is provided by

$$|A_e| = \sqrt{-\frac{\text{real}(a_1)}{\text{real}(a_2)}}. \tag{3.13}$$

Because the values of δ are very small, the results of the present weakly nonlinear analysis are almost coincident with those discussed in [17], and the interested reader is referred to [17] for a thorough discussion of the ripple characteristics as a function of the parameters of the problem.

4. The results of the nonlinear analysis

The results obtained from (3.13) can be useful to quantify the regions in the parameter space where rolling-grain ripples are stable and those where they are unstable, and the development of small bottom perturbations leads to the appearance of vortex ripples. Indeed, if initial perturbations of infinitesimal amplitude are considered and the parameters of the problem are such that the real part of a_2 is negative, nonlinear effects cause the perturbation to reach an equilibrium amplitude $|A_e|$ equal to $\sqrt{-\text{real}(a_1)/\text{real}(a_2)}$. On the other hand, if the parameters are such that the real part of a_2 is positive, no equilibrium amplitude exists and the perturbation tends to grow indefinitely. In the latter case, the bottom boundary layer separates from the crests of the small amplitude bedforms and vortex ripples appear. As suggested by Sleath [1], vortex ripples appear also in the former case, when $|A_e|$ is such that the ratio between ripple height and length is larger than 0.1.

As already pointed out, the values of a_1 and a_2 differ from those determined by Vittori & Blondeaux [17] of an amount of $O(\delta)$. Because the value of the parameter δ is usually quite small, we argue that the investigation of $O(\delta)$ effects on the coefficients a_1, a_2 and the solution (3.13) of equation (3.11) is not useful. In fact, the results concerning the region of existence of rolling-grain ripples and vortex ripples in the parameter space are only marginally affected by the uniform steady streaming. On the other hand, it is interesting to look at the $O(\delta)$ correction of the value of $C_2^{(0)}$ predicted by Vittori & Blondeaux [17], because $O(\delta)$ terms in $C_2^{(0)}$ cause qualitative changes in the bottom profile. In fact, η is no longer symmetric with respect to the crests and the troughs, because $C_2^{(0)}$ has an imaginary part of $O(\delta)$. Figure 5 shows the equilibrium profile of the ripples obtained by means of the theory for fixed values of the parameters along with that obtained neglecting $O(\delta)$ effects. The characteristic profile of sea ripples affected by a steady current can be recognized from the lee side of the ripples being steeper than the stoss side. Of course, in figure 5, the steady velocity component is from the right to the left. In this case, the symmetry index l_2^*/l_1^* turns out to be 1.81. The experimental data of K. W. Tietze (1979, personal communication to J.R.L. Allen) and [5,6,10], which were obtained using sand, and those described in [4], which were obtained using high density plastic particles, show that the symmetry index increases as the ratio between the steady velocity component and the amplitude of the oscillating one increases, but a limiting value exists. The same dependence is observed in the theoretical results presented in figure 6. The reader should note that the value of u_s^*/U_0^* for a monochromatic wave is equal to $3\pi a^*/(2L^* \sinh[2\pi h^*/L^*])$ or alternatively $(\frac{3}{4})\pi\delta Re$. The analysis shows that the value of the ratio l_2^*/l_1^* is affected by the other parameters of the problem and in particular by those related to sediment characteristics. Note that in figure 6 the symmetry index is plotted increasing δ for fixed values of R_d, Re and different values of $(F_d - F_{dc})/F_{dc}$. Interestingly, for strong steady currents, the different curves tend to converge towards a common value that appears to be the maximum value of the symmetry index and ranges between 2 and 3. A quantitative comparison between experimental observations and theoretical findings can be made looking at table 2, which shows the values of l_2^*/l_1^* detected during experiment numbers 39, 40, 42 of Blondeaux *et al.* [4] along with the theoretical values computed for the same parameters of the problem.

For experiment numbers 30, 35, 36, 41, the theory predicts the formation of vortex ripples, and hence the symmetry index cannot be computed. Indeed, either the value a_2 in (3.13) is positive or the ratio between the height and the length of the ripples turns out to be larger than 0.1 [1]. Vortex ripples were indeed experimentally observed during experiment

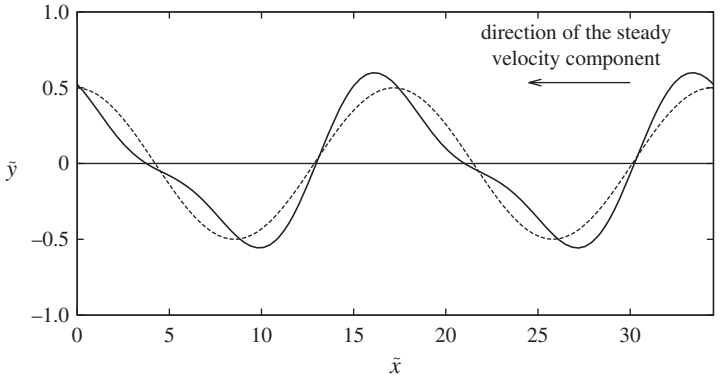

Figure 5. Equilibrium profile of the ripples obtained with the present model for $Re = 15$, $R_d = 25$, $(F_d - F_{dc})/F_{dc} = 0.1$, $\alpha = 0.364$, $\delta = 0.004$ (solid line, considering $O(\delta)$ effects; dashed line, neglecting $O(\delta)$ effects). The ratio between the ripple height h_r^* and the ripple wavelength l_r^* is about 0.067. The value of ψ_d is related to F_d by $\psi_d = F_d^2$.

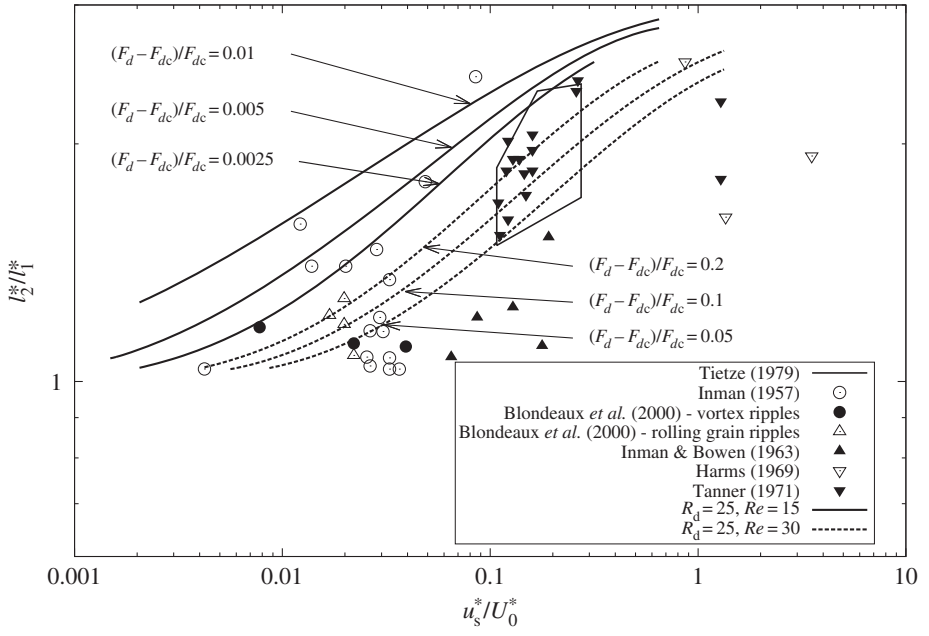

Figure 6. Theoretical value of the symmetry index plotted versus u_s^*/U_0^*, where the value of u_s^*/U_0^* for a monochromatic wave is assumed to be $3\pi\,\delta Re/4$. $R_d = 25$ and $Re = 15, 30$ are values characteristic of Blondeaux *et al.* [4] experiments. The experimental data of figure 1 are also shown. The values of ψ_d are related to F_d by $\psi_d = F_d^2$.

Table 2. Experimental and theoretical values of l_2^*/l_1^* for the experiments of Blondeaux *et al.* [4] characterized by the presence of rolling grain ripples.

experiment number	$(l_2^*/l_1^*)_{exp.}$	$(l_2^*/l_1^*)_{theor.}$
39	1.19	1.17
40	1.23	1.17
42	1.30	1.20

numbers 30, 35, 36. Thus, only the characteristics of the ripples measured during experiment number 41 disagree with those obtained by the theoretical analysis. As previously pointed out, because the theoretical work is based on a weakly nonlinear analysis, it does not allow the description of large amplitude ripples. Clearly, if the parameters of the problem move far away from the marginal conditions and the ripple amplitude obtained by the theory grows, nonlinear effects become stronger, until the perturbation approach fails. Therefore, the theoretical results obtained in this study strictly concern the early stages of ripple formation and the equilibrium configuration of rolling-grain ripples. No theoretical information can be gained on vortex ripples that are characterized by such large amplitudes that flow separation is induced and large vortex structures characterized by a highly nonlinear dynamics are generated. In these cases, the difficulties of the problem call for a numerical solution and an extension of the works reported in [30,31]. Accounting for the presence of a steady drift would be quite useful and would help to understand the basic mechanism of cross-shore sediment transport in that part of the nearshore region characterized by the presence of sea ripples.

5. Discussion and conclusion

Ripple formation underneath a sea wave is analysed retaining nonlinear terms in momentum equation to account for the presence of a steady drift. The ripple profile is no longer symmetric with respect to ripple crests and troughs, and the symmetry index is computed. The main assumptions and the limitations of the analysis are discussed both in the introduction and in §§2–3. However, there are further points that need to be clarified.

As in [17], the flow regime is supposed to be laminar. This assumption might appear to limit the applicability of the analysis to field cases. However, the results described in [21,32] show that the boundary layer at the bottom of sea waves may remain laminar over a wide range of field conditions, and the laminar flow is still a reasonable approximation for moderate values of the Reynolds number such that turbulence appears during the decelerating phases of the cycle, but the flow re-laminarizes during the accelerating phases. Moreover, to neglect the effects that the vortex structures shed by the sediment grains have on the flow, the grain size should be much smaller than the thickness of the bottom boundary layer. By considering wind waves and fine sand, this assumption is reasonably satisfied.

Another point regards the issue of whether the uncertainty in the sediment transport relationship, which may be larger than the perturbation parameters, makes the asymptotic analysis still significant. In order to discuss this point, it is first necessary to point out that the assumption of bottom perturbations of small amplitude allows the problem, describing a propagating sea wave over a cohesionless bottom (the basic state), to be decoupled from that describing the time development of ripples (the perturbation).

First, the analysis solves the problem for the sea wave. As already discussed, because the time scales of the hydrodynamic and morphodynamic problems are vastly different, the bottom configuration differs from the flat one by a negligible amount. Hence, with the assumptions described in §3, the velocity field can be solved exactly while the amount of sediment moved by the wave can be quantified only with some uncertainty, because the sediment transport predictor is highly idealized.

Moreover, the analysis tackles the problem for the ripples. The perturbations of the basic flow, they induce, are determined exactly by assuming the ripple amplitude to be small. Then, the time development of the bottom configuration is obtained by a sediment balance, which provides ordinary differential equations for the amplitudes of the different spatial components of the bed level. The coefficients of these differential equations are known with some uncertainty because of the uncertainty in the sediment transport predictor. It follows that the results for the vertical displacement of the bottom and, hence, of ripple characteristics are affected by a significant relative error. However, the latter cannot be much larger than that affecting the sediment transport prediction. Therefore, even though the analysis cannot determine ripple characteristics exactly,

it certainly helps to understand the process leading to ripple formation. Moreover, at least, it provides the range within which fall (i) the critical conditions for ripple appearance, (ii) the ripple wavelength, (iii) the ripple migration speed, and (iv) the ripple asymmetry index.

Funding statement. This research was supported by the Italian Ministry of University and Research in the framework of the programme PRIN 2012 titled: 'Modellazione di processi idromorfodinamici costieri per applicazioni ingegneristiche'.

References

1. Sleath JFA. 1984 *Sea bed mechanics*. London, UK: John Wiley & Sons.
2. Nielsen P. 1992 *Coastal bottom boundary layers and sediment transport*. Singapore: World Scientific.
3. Allen JRL. 1984 *Sedimentary structures, their character and physical basis*. Amsterdam, The Netherlands: Elsevier.
4. Blondeaux P, Foti E, Vittori G. 2000 Migrating sea ripples. *Eur. J. Mech. B* **19**, 285–301. (doi:10.1016/S0997-7546(90)00106-I)
5. Inman DL. 1957 Tech. Mem. U.S. Beach Erosion N. 100.
6. Tanner WF. 1971 Numerical estimates of ancient waves, water depth and fetch. *Sedimentology* **16**, 71–88. (doi:10.1111/j.1365-3091.1971.tb00219.x)
7. Allen JRL. 1979 A model for the interpretation of wave ripple-marks using their wavelength textural composition and shape. *J. Geol. Soc. Lond.* **36**, 673–683. (doi:10.1144/gsjgs.136.6.0673)
8. Longuet-Higgins MS. 1953 Mass transport in water waves. *Phil. Trans. R. Soc. Lond. A* **345**, 535–581. (doi:10.1098/rsta.1953.0006)
9. Inman DL, Bowen AJ. 1963 Flume experiments on sand transport by waves and currents. In *Proc. 8th Conf. on Coastal Engineering, Mexico City, Mexico, November 1962*, pp. 137–150.
10. Harms JC. 1969 Hydraulic significance of some sand ripples. *Bull. Geol. Soc. Am.* **80**, 363–396. (doi:10.1130/0016-7606(1969)80[363:HSOSSR]2.0.CO;2)
11. Lyne WH. 1971 Unsteady viscous flow over a wavy wall. *J. Fluid Mech.* **50**, 33–48. (doi:10.1017/S0022112071002441)
12. Sleath JFA. 1976 On rolling-grain ripples. *J. Hydraul. Res.* **14**, 69–81. (doi:10.1080/00221686709499689)
13. Blondeaux P. 1990 Sand ripples under sea waves. I. Ripple formation. *J. Fluid Mech.* **218**, 1–17. (doi:10.1017/S0022112090000908)
14. Blondeaux P, Vittori G. 1991 Vorticity dynamics in an oscillatory flow over a rippled bed. *J. Fluid. Mech.* **226**, 257–289. (doi:10.1017/S0022112091002380)
15. Hara T, Mei CC. 1990 Oscillating flows over periodic ripples. *J. Fluid Mech.* **211**, 183–209. (doi:10.1017/S0022112090001549)
16. Hara T, Mei CC. 1990 Centrifugal instability of an oscillatory flow over periodic ripples. *J. Fluid Mech.* **217**, 1–32. (doi:10.1017/S002211209000060X)
17. Vittori G, Blondeaux P. 1990 Sand ripples under sea waves. II. Finite amplitude development. *J. Fluid Mech.* **218**, 19–39. (doi:10.1017/S002211209000091X)
18. Vittori G, Blondeaux P. 1992 Sand ripples under sea waves. Part 3. Brick-pattern ripple formation. *J. Fluid Mech.* **239**, 23–45. (doi:10.1017/S0022112092004300)
19. Roos PC, Blondeaux P. 2001 Sand ripples under sea waves. IV. Tile ripple formation. *J. Fluid Mech.* **447**, 227–246. (doi:10.1017/S0022112001005961)
20. Hara T, Mei CC, Shum KT. 1992 Oscillating flow over periodic ripples of finite slope. *Phys. Fluids* **4**, 1373–1384. (doi:10.1063/1.858414)
21. Blondeaux P, Vittori G. 1999 Boundary layer and sediment dynamics under sea waves. In *Advances in coastal and ocean engineering*, vol. 4 (ed. PLF Liu), pp. 133–190. Singapore: World Scientific.
22. Blondeaux P. 2001 Mechanics of coastal forms. *Annu. Rev. Fluid Mech.* **33**, 339–370. (doi:10.1146/annurev.fluid.33.1.339)
23. Colombini M, Stocchino A. 2011 Ripple and dune formation in rivers. *J. Fluid Mech.* **673**, 121–131. (doi:10.1017/S0022112011000048)
24. Fredsøe J, Deigaard R. 1992 *Mechanics of coastal sediment transport*. Singapore: World Scientific.
25. Mei CC. 1989 *The applied dynamics of ocean surface waves*. Singapore: World Scientific.
26. Vittori G, Blondeaux P. 1996 Mass transport under sea waves over a rippled bed. *J. Fluid Mech.* **314**, 247–265. (doi:10.1017/S0022112096000304)

27. Ursell F. 1953 The long-wave paradox in the theory of gravity waves. *Proc. Camb. Phil. Soc.* **49**, 685–694. (doi:10.1017/S0305004100028887)
28. Grass JA, Ayoub RNM. 1982 Bed load transport of fine sand by laminar and turbulent flow. In *Proc. 18th Conf. on Coastal Engineering, Cape Town, South Africa, 14–19 November 1982*, pp. 1589–1599.
29. Blondeaux P, Sleath JFA, Vittori G. 1988 Experimental data on sand ripples in an oscillatory flow. Report 01/88, Institute of Hydraulics, University of Genoa.
30. Blondeaux P, Vittori G. 1990 Oscillatory flow and sediment motion over a rippled bed. In *Proc. 22nd Conf. on Coastal Engineering, Delft, The Netherlands, 2–6 July 1990*, pp. 2186–2199.
31. Hansen EA, Fredsøe J, Deigaard R. 1994 Distribution of suspended sediment over wave generated ripples. *J. Waterway Port Coastal Ocean Eng.* **120**, 37–55. (doi:10.1061/(ASCE)0733-950X(1994)120:1(37))
32. Sleath JFA. 1990 Sea bed boundary layers. In *The sea* (ed. BL Le Méhauté, DM Hanes). London, UK: Wiley.